RSC Advances

ROYAL SOCIETY OF CHEMISTRY

PAPER

View Article Online
View Journal | View Issue

Cite this: *RSC Adv.*, 2026, **16**, 8401

First-principles insights into half-metallic ferromagnetism, lattice dynamics, and thermoelectric performance of MgX_2Se_4 (X=Ti, Mn) spinel chalcogenides

Ashiq Ramzan, Mudasir Younis Sofi, Mohd. Shahid Khan and M. Ajmal Khan *

Half-metallic ferromagnets are central to spintronic and energy-conversion technologies due to their high spin polarization and multifunctional transport behavior. In this study, a first-principles investigation based on density functional theory within the GGA framework employing the modified Becke–Johnson potential is carried out to examine the structural, electronic, magnetic, optical and thermoelectric properties of the spinel chalcogenides $MgTi_2Se_4$ and $MgMn_2Se_4$. Total-energy calculations identify the ferromagnetic configuration as the ground state for both compounds. The negative formation enthalpies and phonon dispersion spectra free of imaginary frequencies confirm their thermodynamic and dynamical stability. Electronic band-structure analysis reveals half-metallicity arising from strong hybridization between transition-metal-d and Se-p orbitals, which is characterized by metallic behavior in the spin-up channel and a semiconducting gap in the spin-down channel. This electronic structure yields integer magnetic moments of 4 μ_B per formula unit for $MgTi_2Se_4$ and 16 μ_B per formula unit for $MgMn_2Se_4$ and is consistent with half-metallic ferromagnetism. The calculated elastic constants satisfy the Born stability criteria, confirming mechanical stability. The materials exhibit intrinsic ductility and pronounced elastic anisotropy. High elastic moduli, sound velocities and Debye temperatures further indicate enhanced lattice rigidity and high thermal stability. Optical properties derived from the complex dielectric function reveal large static dielectric constants. Strong interband transitions lead to intense ultraviolet absorption and high optical conductivity. These features indicate efficient electron–photon coupling. Spin-resolved transport analysis reveals pronounced Seebeck asymmetry, confirming dominant majority-spin carrier transport. The combined effects of finite Seebeck coefficients, relatively high electrical conductivity and suppressed lattice thermal conductivity lead to enhanced thermoelectric performance under n-type doping, with the dimensionless figure of merit reaching $ZT \approx 0.9$ for $MgTi_2Se_4$ and $ZT \approx 0.99$ for $MgMn_2Se_4$ at room temperature. These results establish $MgTi_2Se_4$ and $MgMn_2Se_4$ as promising multifunctional materials for spintronic, spin-caloritronic, and energy-harvesting applications.

Received 25th November 2025
Accepted 2nd February 2026

DOI: 10.1039/d5ra09092j

rsc.li/rsc-advances

1 Introduction

The search for multifunctional materials capable of addressing both energy and technological demands has intensified due to the growing global emphasis on sustainable energy solutions and advanced electronic systems.[1] Simultaneously, the advancement of spin-based electronics relies critically on achieving high spin polarization in solid-state materials.[2,3] Moreover, increasing environmental and economic concerns necessitate the development of non-toxic, earth-abundant, and cost-effective materials to ensure ecological safety and large-scale applicability.[4–6] Among the diverse material classes explored, spinel-type chalcogenides have attracted significant attention owing to their excellent mechanical robustness, tunable electronic characteristics, and high structural flexibility.[7–10] In particular, thiospinels with the general chemical formula AB_2X_4 (where A is a divalent cation, B is a transition or rare-earth metal, and X = S or Se) typically crystallize in a cubic spinel structure and exhibit a wide range of functional properties, including magnetic ordering, metal–insulator transitions, superconductivity, structural phase transitions, and notable thermoelectric responses.[11–14] Recent first-principles investigations on chalcogenide spinel systems such as $CdTi_2X_4$ (X = S, Se), $MgSm_2(S/Se)_4$, and rare-earth-based $CdGd_2(S/Se)_4$ have reported ferromagnetic semiconducting and half-metallic behaviour, along with promising transport and thermoelectric characteristics, underscoring the multifunctional nature of these materials.[15–17] The magnetic behaviour in these systems primarily originates from strong

Department of Physics, Jamia Millia Islamia, New Delhi-110025, INDIA. E-mail: majkhan@jmi.ac.in

hybridization between chalcogen p orbitals and transition-metal or rare-earth d/f orbitals, which plays a key role in stabilizing spin-polarized electronic states.[18–20] A particularly attractive feature of several spinel chalcogenides is half-metallic ferromagnetism (HMF),[21] characterized by 100% spin polarization at the Fermi level, with metallic conductivity in one spin channel and semiconducting or insulating behaviour in the other. This property is highly desirable for spintronic applications such as spin injection, spin filtering, and polarized current transport in semiconductor-based devices.[22,23] Beyond magnetism, spinel chalcogenides have also emerged as promising candidates for thermoelectric energy conversion. The efficiency of thermoelectric materials is quantified by the dimensionless figure of merit $zT = S^2\sigma T/\kappa$, where S is the Seebeck coefficient, σ is the electrical conductivity, and κ represents the total thermal conductivity.[24–26] Enhancing zT typically involves band-gap engineering and phonon-scattering mechanisms to suppress lattice thermal conductivity. Several transition-metal-based thiospinels, including $HgY_2(S/Se)_4$, $ZnMn_2(S/Se/Te)_4$, $Mg(Lu/La)_2Z_4$ (Z = S, Se), SrX_2S_4 (X = Mn, Fe, Co), as well as $MgNi_2S_4$ and $MgNi_2Se_4$, have been recently identified as promising candidates for thermoelectric and spintronic applications.[27–30] Furthermore, intriguing magnetic and electronic phenomena have been reported in spinel systems containing transition metals such as Ti, V, Cr, and Mn, as well as doped Sr–S-based compounds.[31] Despite these advances, magnesium-based thiospinels remain comparatively underexplored, despite their appealing advantages of low toxicity, elemental abundance, and lightweight nature. Motivated by these considerations, the present work employs density functional theory (DFT) to conduct a comprehensive first-principles investigation of $MgTi_2Se_4$ and $MgMn_2Se_4$ thiospinels. The electronic band structures are analyzed using the modified Becke–Johnson (mBJ) potential, known for its reliable prediction of band gaps and exchange splitting in correlated systems. Additionally, thermoelectric properties are evaluated within the Boltzmann transport framework under the constant relaxation time approximation to capture carrier-dependent transport behaviour. The results demonstrate that both $MgTi_2Se_4$ and $MgMn_2Se_4$ exhibit a favorable combination of strong spin polarization, half-metallic ferromagnetism, and promising thermoelectric performance, highlighting their potential for future spintronic and energy-conversion technologies and motivating further experimental exploration.

2 Computational details

Density functional theory (DFT) provides a robust and widely adopted framework for exploring the intrinsic properties of materials across diverse applications. In this study, the electronic and magnetic properties of $Mg(Ti/Mn)_2Se_4$ spinel compounds were investigated using the WIEN2k code, employing the full-potential linearized augmented plane wave (FP-LAPW) method.[32] Structural optimization and total-energy calculations were performed for both ferromagnetic (FM) and non-magnetic (NM) configurations within the generalized gradient approximation (GGA) using the Perdew–Burke–Ernzerhof (PBE) functional.[33] While PBE reliably predicts equilibrium lattice parameters and relative energy trends, it is known to underestimate band gaps and related electronic properties. Although GGA + U was employed to account for on-site Coulomb interactions it induces only minute changes in the band gap. To overcome this limitation and obtain a more accurate description of the electronic structure, the Tran–Blaha modified Becke–Johnson (TB-mBJ) potential was employed.[34] The TB-mBJ potential serves as a computationally efficient alternative to more demanding approaches such as PBE + U and hybrid functionals (*e.g.*, HSE06), offering improved accuracy in predicting band gaps and density of states. Given the relatively moderate electronic correlations among the Ti/Mn-3d, Mg, and Se states in the present compounds, the TB-mBJ scheme was deemed appropriate, providing reliable results at a substantially reduced computational cost. In the FP-LAPW formalism, the crystal was partitioned into muffin-tin spheres and an interstitial region; the wavefunctions were expanded in spherical harmonics within the muffin-tin spheres and in plane waves in the interstitial space. Brillouin-zone integration was carried out using a $12 \times 12 \times 12$ Monkhorst–Pack k-point mesh. The plane-wave cutoff was set to $K_{max} \times R_{MT} = 8.0$, with a maximum angular momentum $\ell_{max} = 10$, and total-energy convergence was achieved within 0.1 mRy. The thermoelectric properties of $Mg(Ti/Mn)_2Se_4$ were evaluated using the BoltzTrap code, which is based on semi-classical Boltzmann transport theory.[35] Temperature-dependent transport coefficients, including the Seebeck coefficient and electrical conductivity, were calculated within the constant relaxation time approximation using well-established transport equations reported in the literature.[36] These parameters provide critical insight into the thermoelectric performance and potential applicability of the studied materials.

$$S = \frac{ek_B}{\sigma}\int\left(\frac{\partial f_0}{\partial \varepsilon}\right)\frac{\varepsilon-\mu}{k_B T}\Xi(\varepsilon)\mathrm{d}\varepsilon \quad (1)$$

$$\sigma = e^2\int\left(-\frac{\partial f_0}{\partial \varepsilon}\right)\Xi(\varepsilon)\mathrm{d}\varepsilon \quad (2)$$

$$\kappa_e = {k_B}^2 T\int\left(\frac{\partial f_0}{\partial \varepsilon}\right)\left(\frac{\varepsilon-\mu}{k_B T}\right)^2\Xi(\varepsilon)\mathrm{d}\varepsilon \quad (3)$$

Here, $\Xi(\varepsilon)$ is a transport distribution function specified by $\Xi^{\alpha,\beta}(\varepsilon) = \sum_k \delta(\varepsilon-\varepsilon_k)v_k^\alpha v_k^\beta \tau_k$.where v_k^αrepresent αth component of the group velocity with wave vector k. For improved output, the k-mesh was expanded to 100 000-k points.

3 Results and discussion

3.1 Structural properties

The spinel-type compounds MgX_2Se_4 (X = Ti, Mn), crystallizes in the cubic spinel structure with space group $Fd\bar{3}m$ (No. 227). There are eight magnesium, sixteen transition metal (Ti/Mn) and thirty-two selenium atoms in each unit cell. In this structure, the tetrahedral 8a Wyckoff positions (0.125, 0.125, 0.125) are occupied by Mg atoms and the octahedral 16d sites (0.5, 0.5,

0.5) are occupied by Ti and Mn atoms. To preserve the cubic symmetry of the structure the Se atoms occupy the 32e Wyckoff positions with fractional coordinates typically optimized around (0.25 0.25 0.25).[37] The optimized crystal structure is shown in Fig. 1(a). To determine the equilibrium structural parameters, total energy *versus* volume (*E*–*V*) curves were generated using the generalized gradient approximation (GGA) as proposed by Perdew–Burke–Ernzerhof (PBE). These data were fitted using the Murnaghan equation of state[38] as:

$$E(V) = E_0 + \frac{9B_0V_0}{16}\left\{\left[\left(\frac{V_0}{V}\right)^{2/3} - 1\right]B_0' + \left[\left(\frac{V_0}{V}\right)^{2/3} - 1\right]^2\left[6 - 4\left(\frac{V_0}{V}\right)^{2/3}\right]\right\}$$

where $E(V)$ is the total energy at volume V, E_0 is the equilibrium total energy, V_0 is the equilibrium volume, B_0 is the bulk modulus and B_0' is its pressure derivative which enables the extraction of key parameters such as the equilibrium volume, bulk modulus, and its pressure derivative. By connecting these physical quantities to the total energy $E(V)$ at a specific volume V, this equation offers a solid understanding of the structural behaviour of the compounds under various volumes. The total energies of the ferromagnetic (FM) and non-magnetic (NM) configurations were compared to assess the magnetic stability of both compounds. The FM phase is energetically more stable as confirmed by the positive energy differences ($\Delta E = E_{NM}$–E_{FM}) suggesting that $MgTi_2Se_4$ and $MgMn_2Se_4$ possess ferromagnetic ground states. The *E*–*V* curves of the FM configurations shown in Fig. 1(b). Exhibit well-defined minima confirming thermodynamic equilibrium and proper structural optimization. Thermodynamic stability was further assessed through the enthalpy of formation (ΔH_f) calculated using $\Delta H_f = \frac{E_{total} - mE_X - nE_{mg} - pE_{Se}}{7}$ where E_{total} is the total energy of the spinel and E_X, E_{Mg} and E_{Se} are the elemental reference energies for Ti/Mn, Mg, and Se, respectively. The calculated formation enthalpies are −0.820 eV for $MgTi_2Se_4$ and −0.579 eV for $MgMn_2Se_4$ both negative values confirming the thermodynamic viability of the compounds. To evaluate structural compatibility within the spinel framework, the tolerance factor (τ) was computed using the formula: $\tau = \frac{\sqrt{3}(R_X + R_{SC})}{2(R_{Mg} + R_{Se})}$ are the ionic radii of Ti/Mn, Mg, and Se, respectively. For $MgTi_2Se_4$ and $MgMn_2Se_4$, the estimated τ values were 0.92 and 0.94. These values suggest a structurally stable cubic configuration because they are close to unity. The structural and thermodynamic robustness of MgX_2Se_4 (X = Ti, Mn) spinels is supported by the near-unity tolerance factor and negative enthalpy of formation. Table 1 reports the calculated values, which are in good agreement with previous theoretical DFT studies.[39] They are therefore excellent options for use in

Table 1 Lattice parameter (Å), bulk modulus (GPa), energies differences (eV), enthalpy of formation eV per atom, spin-down gap ($\downarrow E_g$ (eV)), half-metallic gap, g_{hm} (eV) and spin splitting gap along with tolerance factor are calculated for spinels $MgTi_2Se_4$ and $MgMn_2Se_4$

	Present	Work	Reported	Work[39]
Parameters	$MgTi_2Se_4$	$MgMn_2Se_4$	$MgTi_2S_4$	$MgMn_2S_4$
a_0	10.87	10.89	10.19	10.17
B_0	66.96	55.91	83.17	86.25
ΔE_1	1.33	0.097	—	—
ΔH_f	−0.820	−0.579	−1.22	−0.98
$\downarrow E_g$	1.29	1.86	1.65	2.00
g_{hm}	0.29	1.1	0.15	0.75
Δ_{spin}	2	1.4	—	—
τ	0.92	0.94	—	—

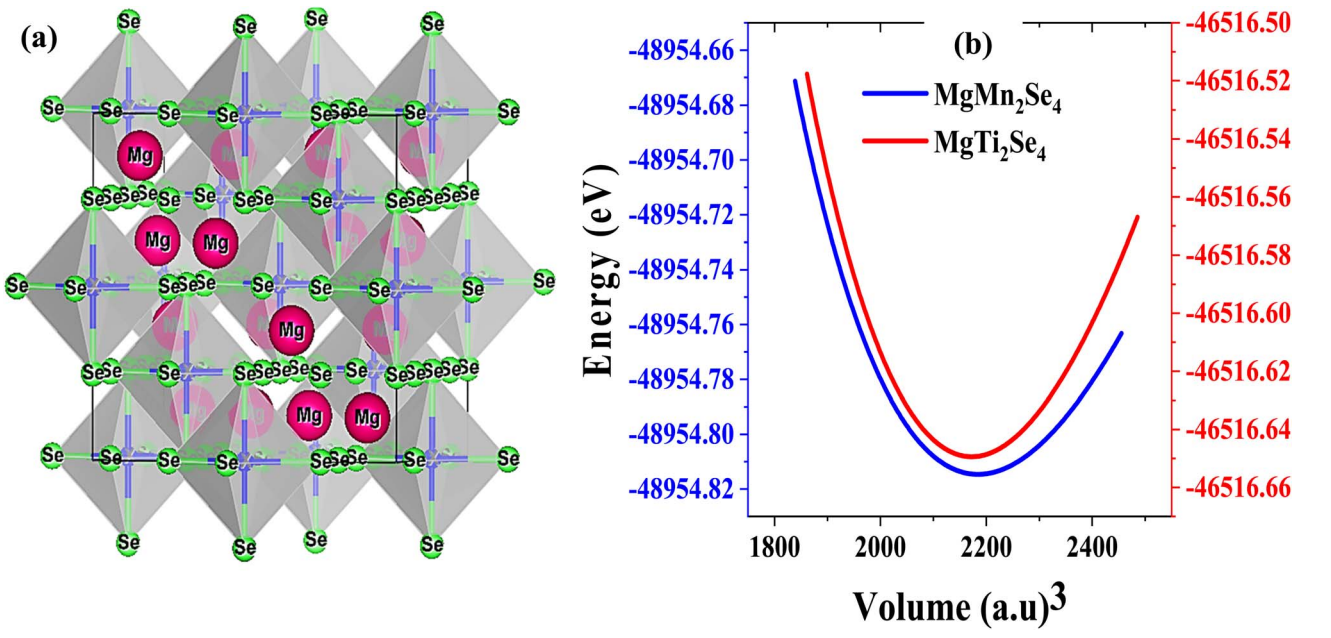

Fig. 1 (a) Crystal structure of the material in the cubic $Fd\bar{3}m$ phase and (b) optimized total energy as a function of volume.

optoelectronic and thermoelectric technologies. Their potential for magnetic and multifunctional device applications is further enhanced by the observed FM ground state. The computed values from our first-principles simulations are shown in Table 1.

3.2 Electronic structure

A material's electronic configuration governs its physical behavior and determines its suitability for a wide range of technological applications. Among electronic parameters the band gap plays a central role as a key tuning factor for optimizing performance in advanced technologies such as spintronics optoelectronics and non-volatile memory devices. In this work the electronic band structures of $MgTi_2Se_4$ and $MgMn_2Se_4$ were calculated using three exchange–correlation approaches namely the generalized gradient approximation GGA + U and the modified Becke–Johnson potential combined with GGA mBJ–GGA. Although the GGA + U method accounts for on-site coulomb interactions it produces only marginal changes in the band gap. Consequently, the final electronic structure analysis is primarily based on the more reliable mBJ–GGA results. A systematic comparison between GGA and mBJ–GGA shows that both approaches predict qualitatively similar electronic features. However, mBJ–GGA yields significantly larger and more realistic band gap values. This improvement highlights the superior capability of the mBJ–GGA functional in describing exchange–correlation effects in transition-metal-based spinel chalcogenides where conventional GGA typically underestimates band gaps due to its limited treatment of localized d-electron interactions. All atomic orbital contributions are included in the band structure calculations providing a comprehensive description of the electronic environment and

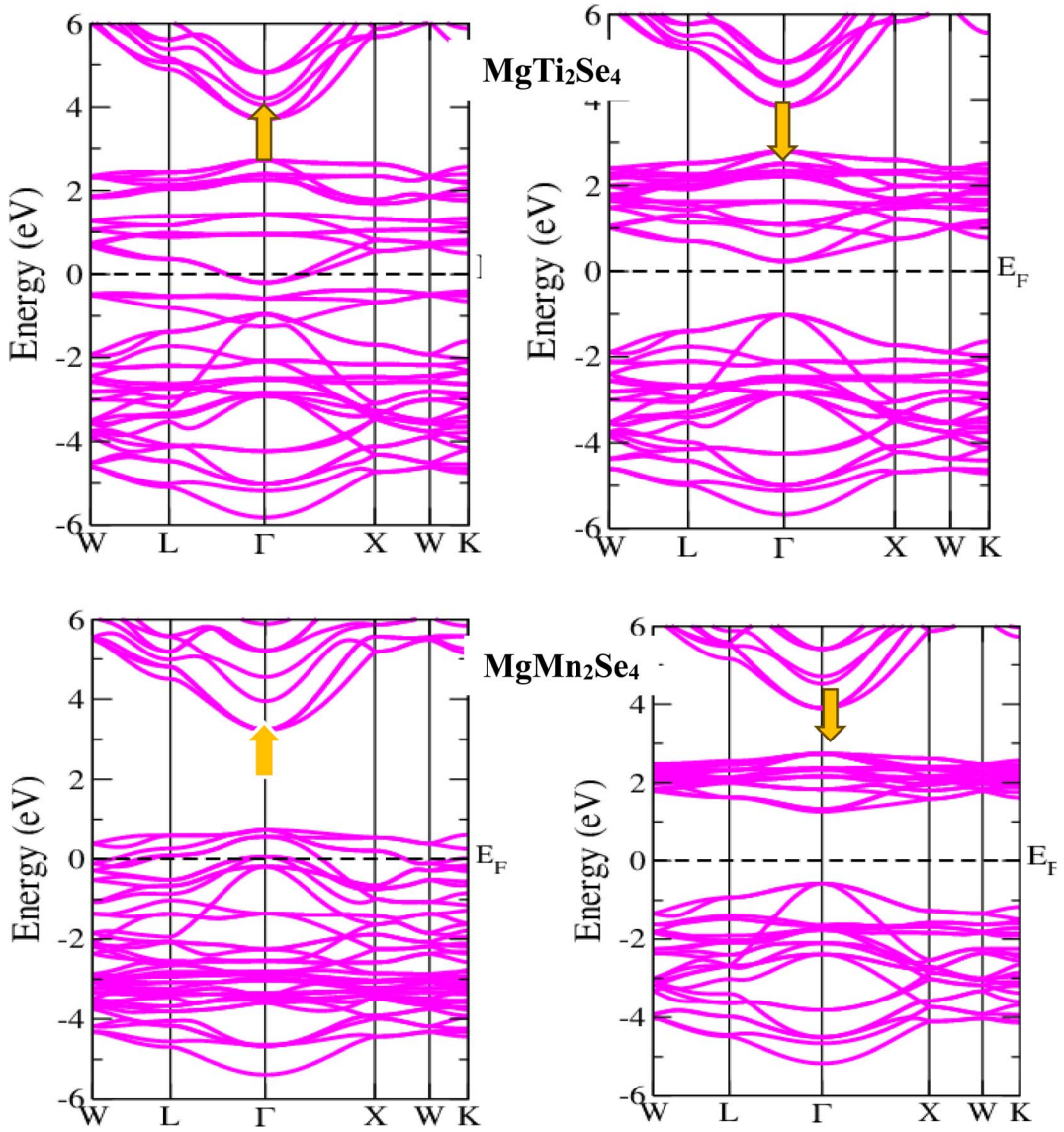

Fig. 2 Plot of electronic band structure for MgX_2Se_4 in spin-up and spin-down channels using the GGA + mBJ potential approximation (X = Ti/Mn).

enabling an accurate assessment of the optoelectronic and spintronic potential of these materials. Both $MgTi_2Se_4$ and $MgMn_2Se_4$ exhibit half-metallic ferromagnetism as shown in Fig. 2 with pronounced spin asymmetry in their band structures. The spin-down minority channel shows semiconducting behavior with the Fermi level located within a clear energy gap whereas the spin-up majority channel exhibits metallic behavior with the Fermi level crossing the valence band. This spin-dependent band distribution confirms 100% spin polarization at the Fermi level which is a defining feature of half-metallicity and is crucial for efficient spin injection and filtering in spintronic devices. Using both functionals the band gap (E_g) defined as the energy difference between the valence band maximum and the conduction band minimum was calculated and is presented in Table 1. The mBJ–GGA results closely match previous theoretical reports[39] confirming the reliability of this approach for spinel-type materials. Spin-dependent features are further emphasized through a detailed analysis of the band dispersion. Charge transport benefits from the more dispersive bands in the spin-up channel, which reflects a lower effective mass and higher carrier mobility. In contrast the flatter bands observed in the spin-down channel indicate higher effective masses which are favorable for spin-selective transport mechanisms but result in reduced charge carrier mobility.[40] Strong exchange interactions essential for stabilizing ferromagnetic ordering give rise to the direct band gap observed in the spin-down channel near the Fermi level. The spin-splitting energy gap defined as the energy difference between the Fermi level and the valence band maximum or conduction band minimum in each spin channel was calculated and is listed in Table 1. Furthermore, the degree of spin polarization (P) at the Fermi level was determined using the expression $P = \frac{N^{\downarrow}(\mathrm{EF}) - N^{\uparrow}(\mathrm{EF})}{N^{\downarrow}(\mathrm{EF}) + N^{\uparrow}(\mathrm{EF})} \times 100$ where $N^{\uparrow}(\mathrm{EF})$ and $N^{\downarrow}(\mathrm{EF})$ represent the density of states (DOS) at the Fermi level for spin-up and spin-down channels, respectively. A result of $P = 100\%$confirms complete spin polarization, a hallmark of half-metallicity.[41] The energy difference between the highest occupied and lowest unoccupied states in the spin-down channel, known as the half-metallic gap (E_{hmg}), was also calculated. Because it controls the stability and robustness of the half-metallic state, this parameter is especially important for spin-filtering and tunnelling magnetoresistance (TMR) applications. These compounds' half-metallic ferromagnetic nature is further supported by the presence of a finite E_{hmg}, highlighting their potential as next-generation magneto-optoelectronic materials, magnetic sensors, and spintronic switches.

3.2.1 Density of states analysis. To gain a detailed understanding of the electronic structure and orbital hybridization mechanisms in $MgTi_2Se_4$ and $MgMn_2Se_4$, the total density of states (TDOS) and partial density of states (PDOS) were systematically analyzed. These analyses provide clear insight into the orbital-resolved contributions to the electronic structure and elucidate the distribution of electronic states over different energy ranges. The calculated TDOS and PDOS spectra, presented in Fig. 3, are in good agreement with the corresponding band structures and validate the reliability of the electronic structure calculations. For $MgTi_2Se_4$, the metallic nature in the spin-up channel originates from strong hybridization between Ti-3d and Se-3p orbitals within the energy window of approximately −2 eV to +2 eV around the Fermi level. In contrast, the spin-down channel exhibits semiconducting behavior, with predominantly localized states distributed between −4.3 eV and −2.5 eV, leading to a clear spin-dependent electronic structure. In $MgMn_2Se_4$, the PDOS reveals pronounced spin asymmetry, where spin-up states are mainly located between −4.2 eV and −2.2 eV, while spin-down subbands extend from −4.1 eV to −2.1 eV. These features indicate that the Mn-3d and Se-4p orbitals play a dominant role in governing both the electronic and magnetic properties of the compound. Moreover, the clear exchange splitting evidenced by the energy separation between spin-up and spin-down states

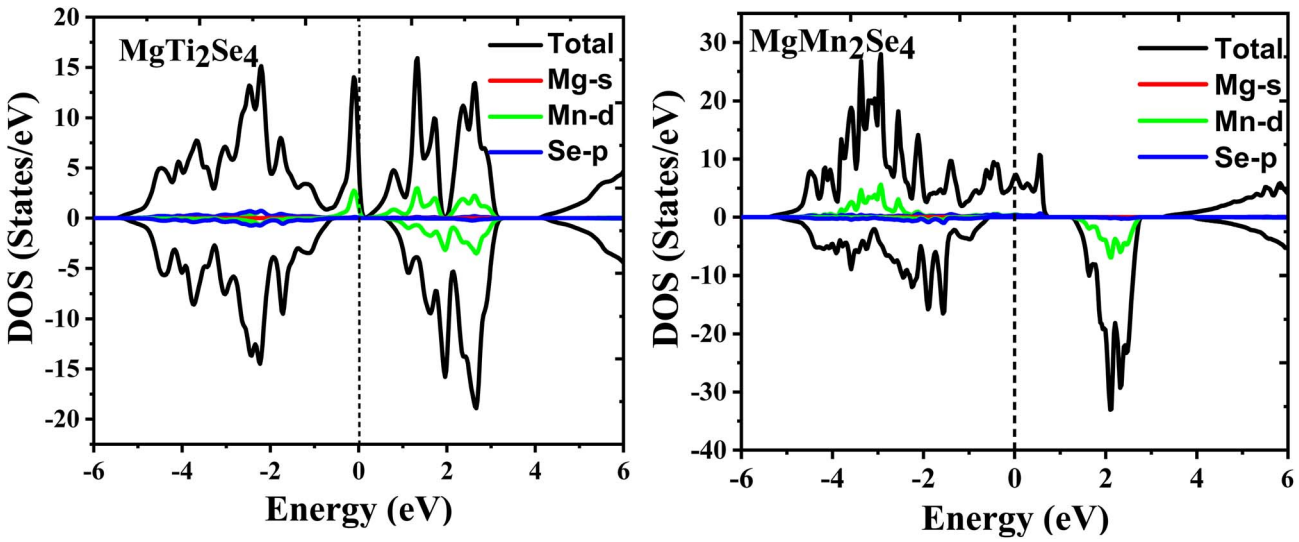

Fig. 3 Plot of total density (TDOS) of states and partial density of states in spin up and spin down channels for MgX_2Se_4 (X = Ti/Mn).

confirms the energetic stability of the ferromagnetic ground state in both materials. The coexistence of complete spin polarization, visible-range band gaps in the spin-down channel, and strong exchange interactions establishes $MgTi_2Se_4$ and $MgMn_2Se_4$ as promising candidates for next-generation spintronic, optoelectronic, and magneto-transport applications.

3.3 Magnetic behaviour

The ferromagnetic nature of $MgTi_2Se_4$ and $MgMn_2Se_4$ spinels was established through spin-polarized DFT-based volume optimization, confirming that both compounds energetically favor a ferromagnetic (FM) ground state. These materials crystallize in the cubic spinel structure with space group $Fd\bar{3}m$, where Mg occupies tetrahedral (A) sites and the transition metals Ti or Mn reside at octahedral (B) sites, each coordinated by six Se atoms. In $MgTi_2Se_4$, although Ti^{4+} ($3d^0$) is formally expected to be nonmagnetic, a finite local magnetic moment of ~0.88762 μB per Ti atom is obtained. Such induced magnetism in nominally d^0 cations has been widely reported and is commonly attributed to strong p–d hybridization between the transition-metal d states and ligand p orbitals, leading to partial occupation and spin polarization of the d states rather than purely ionic Ti^{4+} behavior.[42–45] Under octahedral coordination, the Ti-3d orbitals split into lower-energy t_{2g} and higher-energy e_g states due to crystal-field effects. Spin-resolved partial density of states (PDOS) analysis reveals an exchange splitting of the Ti-t_{2g} states near the Fermi level, confirming that the induced moment originates from hybridization-driven charge transfer from Se-4p states into Ti-3d orbitals. Similar hybridization-induced d^0 magnetism has been previously reported in Ti-based oxides and chalcogenides, where ligand-to-metal charge transfer and covalent bonding give rise to finite magnetic moments on otherwise nonmagnetic cations.[42–44] The reduction of the Ti moment from the ideal 1 μ_B further reflects the itinerant nature of the spin density, which is redistributed into ligand and interstitial regions. This interpretation is supported by the substantial interstitial magnetic moment (0.53244 μ_B) and the negative spin polarization of Se atoms (−0.01283 μB each), a hallmark of p–d hybridization-mediated magnetism.[45] The atomic contributions of Mg (0.00988 μ_B), Ti (0.88762 μ_B), Se (−0.01283 μ_B), and the interstitial region (0.53244 μ_B) yield a total magnetic moment of approximately 4.0004 μ_B per conventional unit cell, consistent with the integer moment expected for half-metallic ferromagnets. This internal consistency between integer magnetization and spin-polarized electronic structure further validates the half-metallicity of $MgTi_2Se_4$. The ferromagnetic exchange interaction in this compound is therefore mediated by hybridization-induced spin polarization and itinerant exchange mechanisms rather than purely localized moments. In contrast, $MgMn_2Se_4$ exhibits strong localized ferromagnetism. Mn^{2+} ions ($3d^5$) adopt a high-spin configuration in an octahedral crystal field, resulting in a large local magnetic moment. The calculated Mn moment of 4.20762 μB is slightly reduced from the ideal 5 μ_B due to p–d hybridization with Se-4p states, as evidenced by the negative Se polarization (−0.13507 μ_B) and a modest interstitial contribution (0.21045 μB). The resulting total magnetic moment of approximately 16.0005 μ_B per unit cell confirms robust ferromagnetic ordering and supports a superexchange-driven Mn–Se–Mn interaction pathway. While $MgMn_2Se_4$ is dominated by localized magnetic moments and strong exchange coupling, the larger interstitial contribution in $MgTi_2Se_4$ indicates more delocalized spin density and weaker, itinerant magnetic interactions.[43] The computed atomic and interstitial magnetic moments for both compounds are summarized in Table 2. These findings not only substantiate the intrinsic ferromagnetism of both materials but also highlight their strong potential for spintronic applications requiring high spin polarization and stable magnetic ordering.

Table 2 The total and partial spin magnetic moments for MgX_2Se_4 (X = Ti/Mn) Spinels

Compound	Total (μ_B)	Int (μ_B)	Mg (μ_B)	Ti/Mn (μ_B)	Se(μ_B)
$MgTi_2S_4$	4.00004	0.53244	0.00988	0.88762	−0.1283
$MgMn_2Se_4$	16.00044	0.21045	0.02003	4.20762	−0.1309

3.4 Elastic properties

The elastic and mechanical properties of the cubic MgX_2Se_4 (X = Ti, Mn) spinel chalcogenides were systematically examined using the second-order elastic constants C_{11}, C_{12}, and C_{44}, as reported in Table 2. In cubic crystals the mechanical stability is governed by the Born stability criteria which require $C_{11} > 0$, $C_{44} > 0$, $C_{11}-C_{12} > 0$, $C_{11} + 2C_{12} > 0$, and $C_{11} > B > C_{12}$.[46] The calculated elastic constants for $MgTi_2Se_4$ and $MgMn_2Se_4$ satisfy all these conditions confirming their mechanical stability in the cubic phase with space group $Fd\bar{3}m$. The relatively larger values of C_{11} compared to C_{12} further indicate strong resistance to uniaxial deformation, while the finite values of C_{44} confirm stability against shear strain. To obtain macroscopic mechanical parameters the elastic constants were converted into bulk shear and Young's moduli using the Voigt–Reuss–Hill approximation which provides reliable estimates for polycrystalline materials.[47–49] The Voigt bulk modulus is defined as $B_V = (C_{11} + 2C_{12})/3$ and for cubic symmetry $B_V = B_R$ where B_R denotes the Reuss bulk modulus. The shear modulus bounds were evaluated using $G_V = (C_{11}-C_{12} + 3C_{44})/5$ and $G_R = 5(C_{11}-C_{12})C_{44}/[4C_{44} + 3(C_{11}-C_{12})]$ with the effective shear modulus given by $G = (G_V + G_R)/2$. The resulting bulk moduli of 66.96 GPa for $MgTi_2Se_4$ and 55.07 GPa for $MgMn_2Se_4$ indicate moderate resistance to uniform compression. In contrast the lower shear moduli of 36.31 GPa and 27.19 GPa respectively indicate that these compounds are more compliant under shear deformation than under volumetric compression. The Young's modulus was calculated using $E = 9BG/(3B + G)$ and attains values of 92.48 GPa for $MgTi_2Se_4$ and 69.65 GPa for $MgMn_2Se_4$, reflecting the comparatively higher stiffness of the Ti-containing compound. The observed trend $E > B > G$ highlights the high stiffness combined with enhanced shear flexibility in these spinel structures. The ductile or brittle nature of the compounds was evaluated using multiple mechanical indicators. According to Pugh's criterion, materials with a ratio $B/G >$

1.75are classified as ductile.[50] The calculated ratios of 1.87 for $MgTi_2Se_4$ and 1.95 for $MgMn_2Se_4$ clearly place both compounds in the ductile regime. This conclusion is further supported by Poisson's ratio, determined from $\nu = (3B–E)/(6B)$, which exceeds the critical value of 0.26 associated with ductile and metallic bonding characteristics.[51] Additionally, the positive Cauchy pressure, defined as $C_{12}–C_{44}$, yields values of 3.7 GPa and 2.5 GPa for $MgTi_2Se_4$ and $MgMn_2Se_4$, respectively, signifying the dominance of non-directional bonding and further confirming their ductile behaviour. Elastic anisotropy, which plays a crucial role in determining crack propagation, mechanical reliability, and direction-dependent response, was analyzed using both the Zener anisotropy factor and the universal anisotropy index. The Zener factor, defined as $A = 2C_{44}/(C_{11}–C_{12})$, deviates significantly from unity, with values of 0.48 for $MgTi_2Se_4$ and 0.37 for $MgMn_2Se_4$, indicating pronounced elastic anisotropy. To provide a more comprehensive measure, the universal anisotropy index was calculated using $A_U = 5(G_V/G_R - 1)$, yielding values of 0.67 and 1.30 for $MgTi_2Se_4$ and $MgMn_2Se_4$, respectively. The larger A_U value for $MgMn_2Se_4$ suggests stronger anisotropic elastic behaviour, particularly in shear-dominated deformation modes. Further insight into the microscopic deformation mechanism was obtained from the Kleinman parameter ξ, which describes the relative ease of bond stretching *versus* bond bending during elastic deformation. The calculated values of 0.37 for $MgTi_2Se_4$ and 0.33 for $MgMn_2Se_4$ indicate a balanced contribution of bond-angle bending and bond-length stretching, implying moderate resistance to angular distortions. In addition, the evaluated sound velocities, Debye temperatures, and thermophysical parameters reveal that $MgTi_2Se_4$ exhibits higher lattice stiffness and thermal robustness compared to $MgMn_2Se_4$, consistent with its larger elastic moduli. We created 3D contour plots for Young's modulus (Y), linear compressibility (β), shear modulus (G), and Poisson's ratio (ν) using the Elate visualization tool to obtain a more thorough grasp of the elastic and anisotropic properties of the compounds under study. These plots illustrate how these properties vary with crystallographic direction and are displayed in Fig. 4 and 5 for MgX_2Se_4 (X = Ti/Mn), respectively. The findings unequivocally demonstrate that all elastic parameters, except for linear compressibility, exhibit a significant deviation from a spherical shape, highlighting their

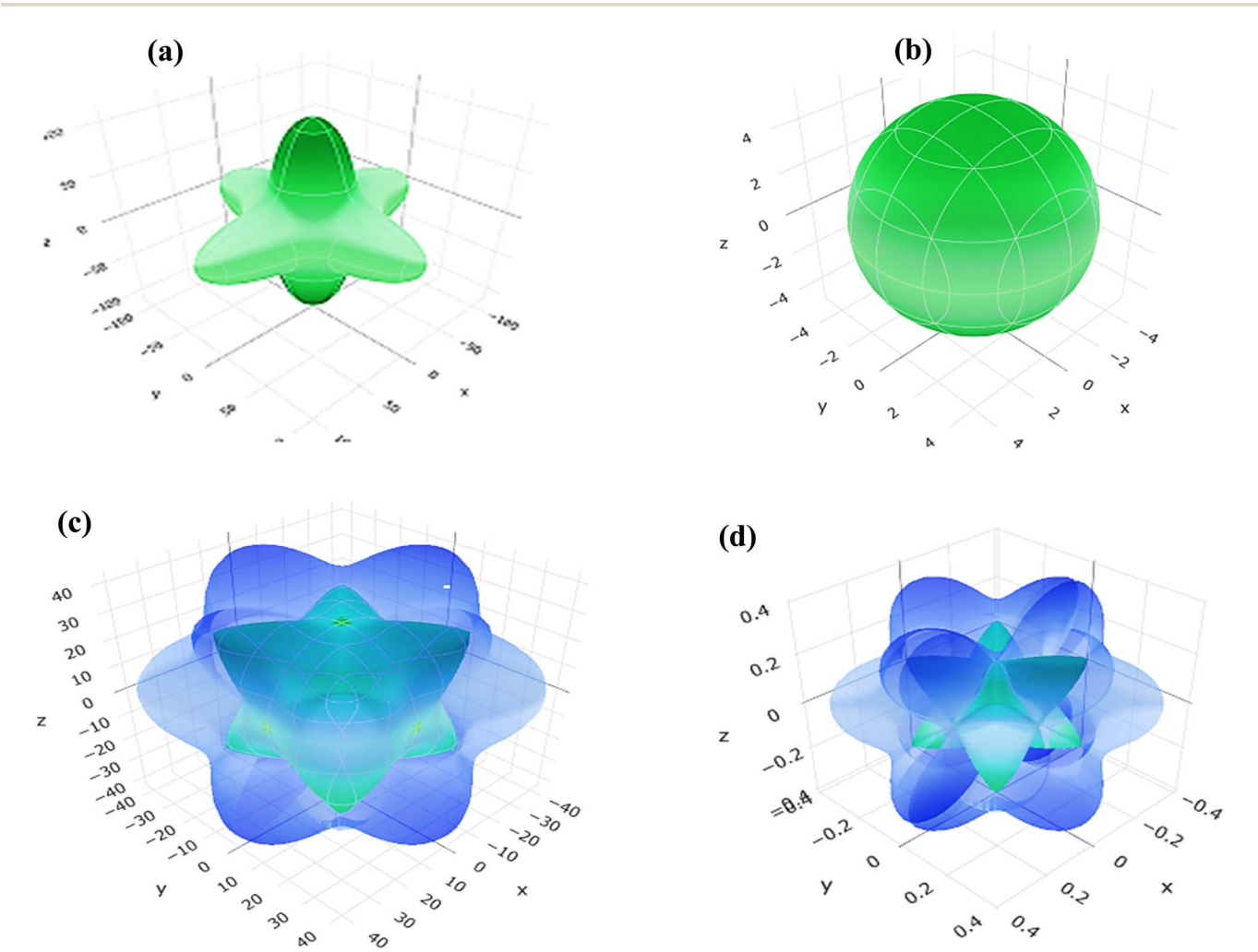

Fig. 4 (a–d) Directional dependence of (a) Young's modulus (Y), (b) linear compressibility (β), (c) shear modulus (G), and (d) Poisson's ratio (ν) for $MgTi_2Se_4$ compound.

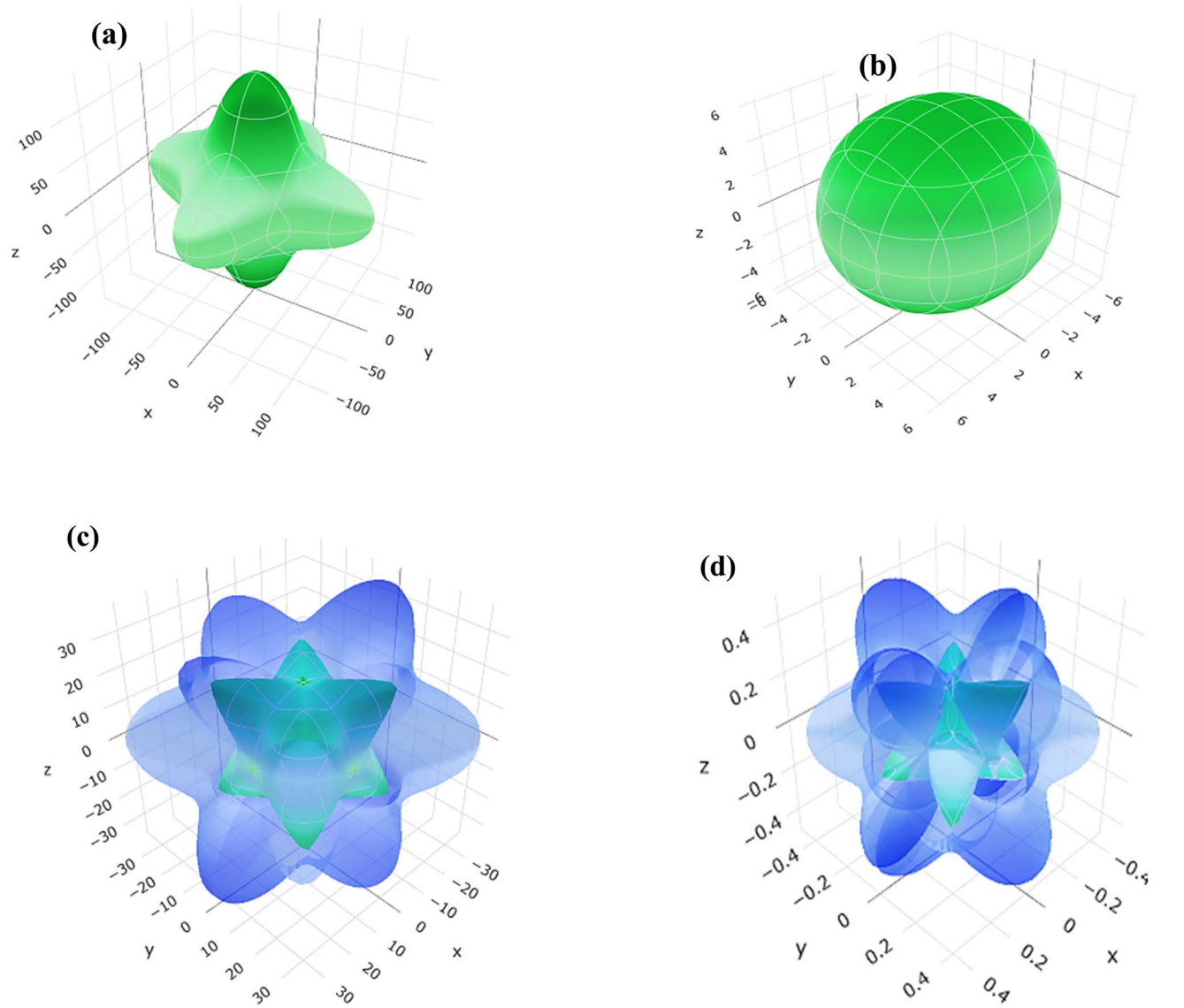

Fig. 5 (a–d) Directional dependence of (a) Young's modulus (Y), (b) linear compressibility (β), (c) shear modulus (G), and (d) Poisson's ratio (ν) for $MgMn_2Se_4$ compound.

anisotropic behaviour. Furthermore, the direction-dependent mechanical response of these spinel structures is confirmed by the anisotropy's uniform distribution across various directions. Table 3 displays the calculated values. Overall, the detailed elastic analysis demonstrates that MgX_2Se_4 (X = Ti, Mn) compounds are mechanically stable, elastically anisotropic, and intrinsically ductile. The combination of moderate stiffness, enhanced shear compliance, and pronounced elastic anisotropy makes these materials promising candidates for technological applications where mechanical reliability, flexibility, and anisotropic response are desirable

3.5 Optical properties

Light is a plentiful, sustainable, and clean energy source with immense potential for next-generation optoelectronic technologies. In recent years, significant attention has been directed toward the development of high-performance materials capable of efficiently harvesting and converting light into electrical energy. The interaction of materials with electromagnetic radiation is primarily governed by electronic transitions induced by photon excitation, which can be classified as intra-band and inter-band transitions. Inter-band transitions, arising from the excitation of electrons from the valence band to the conduction band, play a dominant role in semiconductors and insulators, whereas intra-band transitions occur within the same electronic band and are typically prevalent in metallic systems. Consequently, optical absorption, emission, and the overall photo response of materials are largely dictated by inter-band transitions.[52] The optical properties of $MgTi_2Se_4$ and $MgMn_2Se_4$ were systematically investigated using the complex dielectric function including both the real $\varepsilon_1(\omega)$ and imaginary $\varepsilon_2(\omega)$ components, along with related optical parameters such

Table 3 Elastic, mechanical, and thermophysical properties of $MgTi_2Se_4$ and $MgMn_2Se_4$

Property	Symbol	Unit	$MgTi_2Se_4$	$MgMn_2Se_4$
Elastic constant	C_{11}	GPa	142.6	118
Elastic constant	C_{12}	GPa	30.7	20.5
Elastic constant	C_{44}	GPa	27	18
Bulk modulus	B	GPa	66.96	55.07
Density	ρ	g cm^{-3}	1.82	2.56
Cauchy pressure	C_p	GPa	3.7	2.5
Shear modulus (VRH)	G	GPa	36.31	27.19
Young's modulus	E	GPa	92.48	69.65
Pugh's ratio	B/G	—	1.87	1.95
Poisson's ratio	ν	—	0.273	0.281
Gruneisen parameter	G	—	1.616	1.660
Linear compressibility	B	Pa^{-1}	0.0049	0.0059
Elastic anisotropy factor	A	—	0.48	0.37
Universal anisotropy factor	A_U	—	0.67	1.30
Kleinman parameter	Ξ	—	0.37	0.33
Transverse sound velocity	v_t	km s^{-1}	4.47	3.26
Longitudinal sound velocity	v_l	km s^{-1}	8.00	5.90
Average sound velocity	v_m	km s^{-1}	4.97	3.63
Debye temperature	Θ_D	K	414	339
Melting temperature*	T_m	K	1396	1250
Minimum thermal conductivity*	K_{min}	W m^{-1} K^{-1}	0.47	0.43
Hardness*	H_a	GPa	13.36	10.81

as absorption coefficient, reflectivity, refractive index, and optical conductivity over the photon energy range of 0–14 eV. The imaginary part $\varepsilon_2(\omega)$ represents photon absorption associated with electronic transitions, while the real part $\varepsilon_1(\omega)$ describes the dispersive behavior and the degree of polarization induced by an external electric field. The calculated dielectric functions of $MgTi_2Se_4$ and $MgMn_2Se_4$ are shown in (Fig. 6a and b), respectively. For $MgTi_2Se_4$ (Fig. 6(a)), the static dielectric constant $\varepsilon_1(0)$ is approximately 10, and $\varepsilon_1(\omega)$ decreases with increasing photon energy, becoming negative in the energy range of about 3.5–6 eV, indicating plasmonic-like behavior. The $\varepsilon_2(\omega)$ spectrum exhibits pronounced absorption peaks around 1.5, 3.5, 5, 7, and 10 eV, originating from allowed inter-band electronic transitions. In the case of $MgMn_2Se_4$ (Fig. 6b), the static dielectric constant $\varepsilon_1(0)$ attains a higher value of approximately 35–40, signifying strong low-energy electronic polarization. With increasing photon energy, $\varepsilon_1(\omega)$ rapidly decreases and shows negative values up to nearly 1.5 eV, followed by weak negative regions at higher energies around 12–14 eV, associated with plasmonic-type excitations. The $\varepsilon_2(\omega)$ spectrum displays dominant peaks at approximately 0.5, 2, 4, and 6 eV, corresponding to inter-band transitions, while both $\varepsilon_1(\omega)$ and $\varepsilon_2(\omega)$ gradually diminish at higher photon energies, indicating reduced optical response. These trends are further supported by the optical conductivity spectra shown in (Fig. 6(c). Both compounds exhibit very low optical conductivity below 2 eV, consistent with their optical band gaps. The conductivity increases sharply in the energy range of 2–10 eV and reaches maximum values around 8–10 eV with peak conductivities of approximately 7000 Ω^{-1} cm^{-1} for $MgTi_2Se_4$ and 6500 Ω^{-1} cm^{-1} for $MgMn_2Se_4$, indicating efficient photon-induced charge carrier excitation and strong electron–photon coupling. The absorption coefficient spectra (Fig. 7(d) reveal low absorption in the visible and infrared regions below 3 eV, suggesting optical transparency, followed by strong absorption maxima of about 2.0–2.2 $\times$ 10^6 cm^{-1} in the 12–14 eV range, attributed to high-energy inter-band transitions. $MgTi_2Se_4$ exhibits marginally higher absorption intensity, reflecting stronger transition probabilities. The refractive index $n(\omega)$, derived from $\varepsilon_1(\omega)$ and $\varepsilon_2(\omega)$ and presented in (Fig. 6(e), shows high static values of approximately 8–9 at zero photon energy, indicating strong light–matter interaction and high optical density. In the ultraviolet region, $n(\omega)$ decreases steadily and stabilizes between 2 and 3, reflecting weak dispersion. The extinction coefficient $k(\omega)$, shown in (Fig. 6(f), varies from 1.0 to 2.7 in the energy range of 5–14 eV, confirming the presence of multiple inter-band transitions and complex energy-loss mechanisms Overall, $MgTi_2Se_4$ and $MgMn_2Se_4$ exhibit robust optical responses spanning the visible to ultraviolet regions. Their large static dielectric constants pronounced $\varepsilon_2(\omega)$ peaks, high optical conductivity, and substantial absorption coefficients demonstrate strong electron–photon interactions and high polarizability. The tunability of optical properties through B-site substitution (Ti $\leftrightarrow$ Mn) highlights compositional engineering in spinel chalcogenides as an effective strategy for tailoring materials for advanced optoelectronic, ultraviolet photodetector, solar energy harvesting, and photocatalytic applications. The key optical parameters are summarized in Table 4.

3.6 Transport properties

The thermoelectric effect arises when a temperature gradient is applied across a material resulting in the generation of an

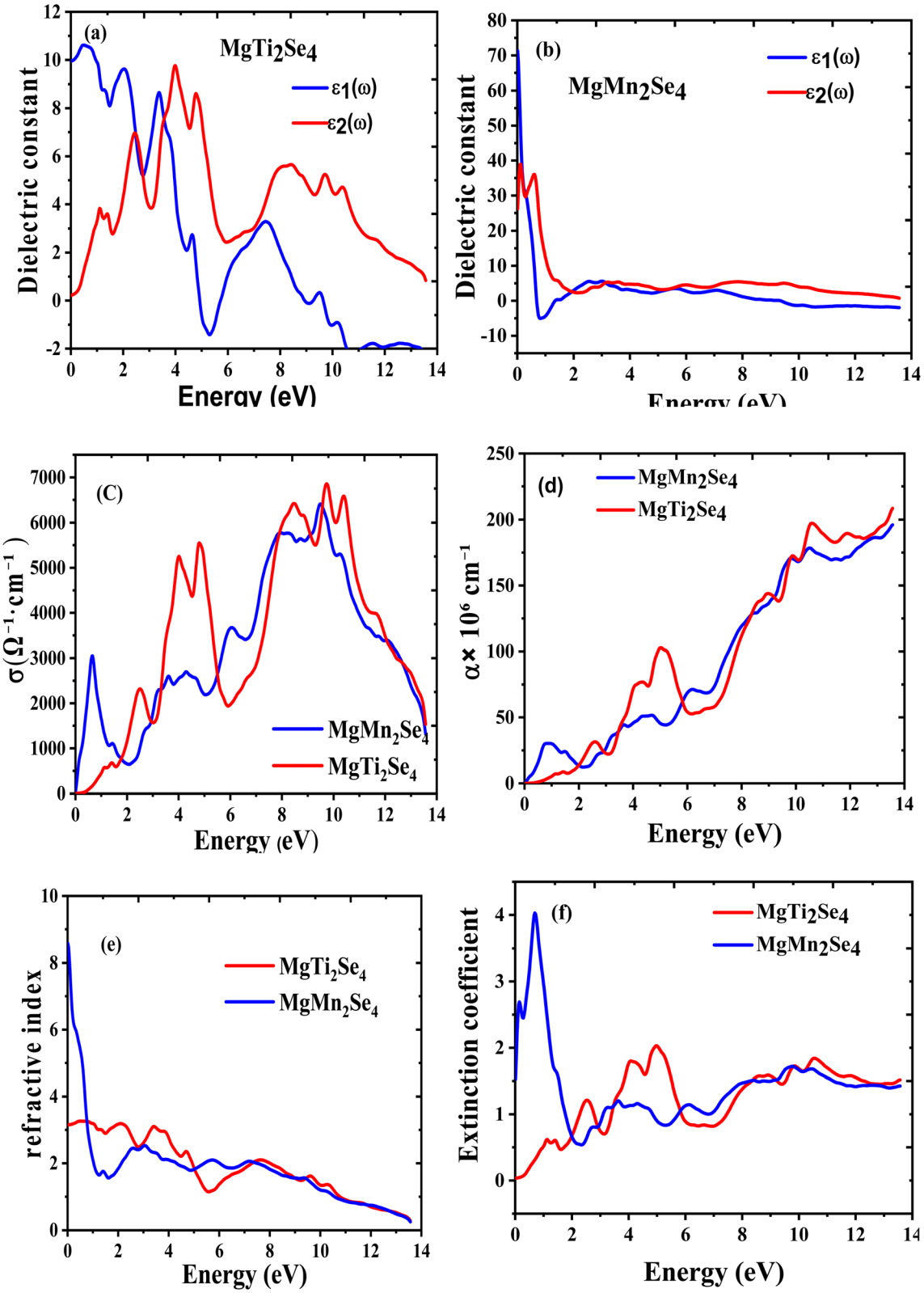

Fig. 6 (a) Represents the real part $\varepsilon_1(\omega)$ and imaginary part $\varepsilon_2(\omega)$ of dielectric constant of $MgTi_2Se_4$ and (b) represents real part $\varepsilon_1(\omega)$ and imaginary part $\varepsilon_2(\omega)$ of dielectric constant of $MgMn_2Se_4$ (c) represents optical conductivity, (d) represents absorption coefficient (e) represents reflective index and (f) excitation coefficient under GGA-mBJ potential approximation.

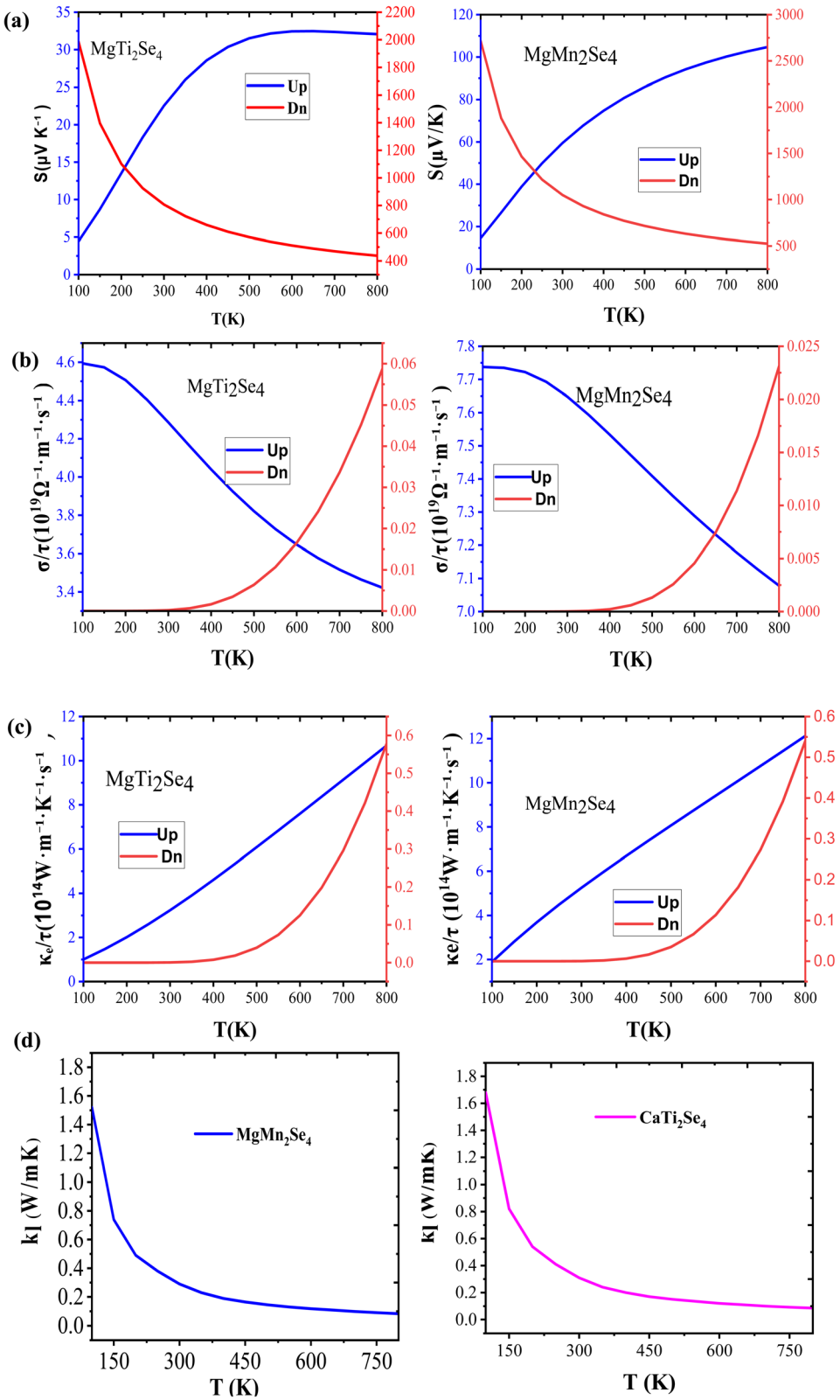

Fig. 7 (a–d) Temperature dependence of (a) the Seebeck coefficient, (b) electrical conductivity (c) total thermal conductivity, and (d) lattice thermal conductivity in the temperature range of 100–800 K.

electric voltage or current. This effect constitutes the fundamental operating principle of thermoelectric devices which are widely employed in temperature control solid-state refrigeration and waste heat recovery for power generation. The performance or efficiency of a thermoelectric material is commonly characterized by the dimensionless figure of merit (zT), expressed as:[53]

$zT = \frac{S^2\sigma T}{\kappa}$, where S is the Seebeck coefficient, σ is the electrical conductivity, κ is the total thermal conductivity (including both electronic and lattice contributions), and T is the absolute temperature. To achieve a high zT value, a material must possess a large Seebeck coefficient and high electrical conductivity, while simultaneously maintaining low thermal conductivity. The electron relaxation time (τ) is the average time between consecutive charge carrier scattering events and is a crucial factor affecting these transport characteristics. The constant relaxation time approximation (CRTA) assumes that the relaxation time varies slowly with energy over a range comparable to the thermal energy (k_BT) and is therefore frequently used in practice. The power factor per unit time ($S^2\sigma/\tau$), electrical conductivity per unit time (σ/τ) and electronic thermal conductivity per unit time (κ_e/τ) are examples of transport coefficients that can be easily expressed in terms of τ under this assumption. Owing to computational limitations, the relaxation time (τ) in this study was assumed to be constant and typically of the order of 10^{-15} seconds, which is consistent with values for semiconducting thermoelectric materials that have been previously reported. As is common in DFT-based thermoelectric studies of related systems a carrier concentration of 1×10^{20} cm^{-3} was chosen. Boltzmann transport theory under the rigid band approximation (RBA) and the constant relaxation time approximation (CRTA) as implemented in the BoltzTraP code[35] was used to evaluate these interdependent transport parameters. Since these compounds are expected to be ferromagnetic the two-current model was also used to investigate how magnetism affects thermoelectric behaviour.[54] This model separates the transport properties into spin-up ($\uparrow$) and spin-down ($\downarrow$) channels, which is essential for capturing spin-dependent scattering and mobility effects that arise due to interactions between conduction electrons and localized magnetic moments. Consequently, the transport quantities become spin-resolved ($S^\uparrow$, $S^\downarrow$, $\sigma^\uparrow$, $\sigma^\downarrow$, $\kappa_e{}^\uparrow$, $\kappa_e{}^\downarrow$), and the total values are computed as $\sigma = \sigma^\uparrow + \sigma^\downarrow$, $\kappa_e = \kappa_e{}^\uparrow + \kappa_e{}^\downarrow$, and $S = \frac{S^\uparrow\sigma^\uparrow + S^\downarrow\sigma^\downarrow}{[\sigma^\uparrow + \sigma^\downarrow]}$. These spin-resolved calculations allow for a more precise understanding of the interplay between magnetism and thermoelectricity in ferromagnetic materials. For possible thermoelectric and spintronic applications, the thermal stability and performance of $MgTi_2Se_4$ and $MgMn_2Se_4$ spinels are clarified by a detailed analysis of the variation of thermoelectric coefficients over the 100–800 K temperature range in the section that follows.

3.6.1 Seebeck coefficient. On applying a temperature gradient (ΔT) across a thermoelectric material, an induced voltage (ΔV) is generated and their ratio defines the Seebeck coefficient (S) according to $\Delta V = S\Delta T$. The magnitude and sign of S are governed by several factors, including operating temperature, carrier concentration, and dominant scattering mechanisms.[55] As illustrated in Fig. 7(a), both $MgTi_2Se_4$ and $MgMn_2Se_4$ exhibit pronounced spin-dependent thermoelectric behavior over the investigated temperature range of 100–800 K. For $MgTi_2Se_4$ Fig. 7(a), the spin-up channel shows a positive Seebeck coefficient, increasing monotonically from approximately 5 μV K^{-1} at 100 K to about 32 μV K^{-1} at 800 K. In contrast, the spin-down channel exhibits a negative Seebeck coefficient with a much larger magnitude, decreasing from roughly −2000 μV K^{-1} at 100 K to about −400 μV K^{-1} at 800 K. The opposite signs and distinctly different temperature dependences of the two spin channels confirm the half-metallic ferromagnetic nature of $MgTi_2Se_4$, indicating hole-dominated transport in the spin-up channel and electron-dominated transport in the spin-down channel. A similar spin-resolved trend is observed for $MgMn_2Se_4$, also shown in Fig. 7(a). The spin-up Seebeck coefficient remains positive and increases steadily from around 15 μV K^{-1} at 100 K to approximately 105 μV K^{-1} at 800 K, suggesting enhanced thermally activated carrier transport with increasing temperature. Meanwhile, the spin-down channel displays a negative Seebeck coefficient, whose magnitude decreases from nearly −3000 μV K^{-1} at 100 K to about −500 μV K^{-1} at 800 K, reflecting a metallic-like transport character at elevated temperatures.

3.6.2 Electrical conductivity (σ). Fig. 7(b) presents the temperature dependence of the electrical conductivity per unit relaxation time (σ/τ), calculated using the BoltzTraP code within the constant relaxation time approximation (RTA). This method allows the evaluation of electronic transport properties without explicitly determining the relaxation time τ and is widely used for comparative thermoelectric studies.[56] Both $MgTi_2Se_4$ and $MgMn_2Se_4$ exhibit pronounced spin-dependent transport behavior over the temperature range of 100–800 K. For $MgTi_2Se_4$, the spin-up channel shows a monotonic decrease in σ/τ with increasing temperature, decreasing from approximately 4.5×10^{19} Ω^{-1} m^{-1} s^{-1} at 100 K to about 3.4×10^{19} Ω^{-1} m^{-1} s^{-1} at 800 K, indicating metallic-like conduction dominated by majority-spin carriers. In contrast, the spin-down conductivity remains nearly zero at low temperatures and begins to increase noticeably above ∼400 K, reaching around 0.06×10^{19} Ω^{-1} m^{-1} s^{-1} at 800 K. This behavior reflects the half-metallic nature of $MgTi_2Se_4$, where electrical transport is primarily governed by the spin-up channel, while minority-spin carriers are thermally activated at elevated temperatures. A similar trend is observed for $MgMn_2Se_4$. The spin-up σ/τ gradually decreases from approximately 7.7×10^{19} Ω^{-1} m^{-1} s^{-1} at 100 K to nearly 7.1×10^{19} Ω^{-1} m^{-1} s^{-1} at 800 K, confirming dominant metallic transport in the majority-spin channel. Meanwhile, the spin-down conductivity remains negligible up to about 450 K, after which it increases rapidly, reaching approximately 0.025×10^{19} Ω^{-1} m^{-1} s^{-1} at 800 K. The delayed yet sharp rise in the minority-spin contribution indicates thermally activated spin-down carriers at higher temperatures.

3.6.3 Thermal conductivity. One of the most important parameters governing thermoelectric efficiency is the thermal conductivity (κ), which quantifies a material's ability to transport heat through both charge carriers and lattice vibrations. In crystalline solids, the total thermal conductivity (κ_{total}) is composed of the electronic contribution (κ_e) and the lattice contribution (κ_l), arising from phonon-mediated heat transport. In the present work, the electronic thermal conductivity per unit relaxation time (κ_e/τ) was evaluated using the BoltzTraP code within the constant relaxation time approximation, while the

Table 4 Key optical properties of $MgTi_2Se_4$ and $MgMn_2Se_4$ from first-principles calculations

Optical parameter	$MgTi_2Se_4$	$MgMn_2Se_4$
Static dielectric constant $\varepsilon_1(0)$	~10–11	~35–40
Dielectric constant at UV (>5 eV)	~4–7	~3–6
Imaginary dielectric peak (energy)	~4.0–4.3 eV	~3.5–3.9 eV
Imaginary dielectric peak (height) ε_2	~9–10	~28–30
Optical conductivity peak (energy)	~7000 Ω^{-1} cm^{-1}	~6500 Ω^{-1} cm^{-1}
Absorption coefficient (at 14 eV)	~2.2 × 10^6 cm^{-1}	~2.0 × 10^6 cm^{-1}
Static refractive index n_0	~8.5	~2.8
Refractive index in UV (5–14 eV)	~2.0–3.0	~1.8–2.8
Energy range of main optical transitions	~3–10 eV	~2.5–9 eV
Extinction coefficient at ~0.5 eV	~4.0	~0.9
Extinction coefficient (5–14 eV)	1.0 to 2.7	1.0 to 2.7
Transparency region (low loss)	<2 eV	<2 eV

lattice thermal conductivity (κ_l) was analyzed separately using slacks model[57,58] as shown in Fig. 7(d). The temperature dependence of κ_e/τ for $MgTi_2Se_4$ and $MgMn_2Se_4$ is presented in Fig. 7(c). For $MgTi_2Se_4$, the spin-up channel exhibits a steady increase in κ_e/τ from approximately 1.0 W m^{-1} K^{-1} s^{-1} at 100 K to nearly 11.0 W m^{-1} K^{-1} s^{-1} at 800 K, indicating enhanced heat transport by majority-spin carriers at elevated temperatures. In contrast, the spin-down contribution remains very small at low temperatures and rises gradually beyond ~400 K, reaching about 0.6 W m^{-1} K^{-1} s^{-1} at 800 K, confirming its comparatively weaker role in thermal transport. A similar trend is observed for $MgMn_2Se_4$, where the spin-up κ_e/τ increases from roughly 2.0 W m^{-1} K^{-1} s^{-1} at 100 K to around 12.0 W m^{-1} K^{-1} s^{-1} at 800 K, while the spin-down channel increases modestly to approximately 0.55 W m^{-1} K^{-1} s^{-1} at the highest temperature. These results indicate that electronic heat transport in both compounds is dominated by the spin-up channel, consistent with their half-metallic ferromagnetic character. The lattice thermal conductivity κ_l, shown in Fig. 7(d), displays a strong temperature-dependent decrease for both compounds, characteristic of enhanced phonon–phonon scattering at elevated temperatures. For $MgTi_2Se_4$, κ_l decreases rapidly from about 1.6 W m^{-1} K^{-1} at 150 K to approximately 0.2 W m^{-1} K^{-1} near 800 K. Similarly, $MgMn_2Se_4$ exhibits a reduction in κ_l from around 1.7 W m^{-1} K^{-1} at 150 K to nearly 0.25 W m^{-1} K^{-1} at 800 K. The low magnitude of κ_l at high temperatures is favorable for thermoelectric applications, as it suppresses parasitic heat flow and helps maintain a large temperature gradient.

3.6.4 Figure of merit (zT). One of the standard parameters used to assess the thermoelectric efficiency of a material is the dimensionless figure of merit (ZT), which describes the effectiveness of converting thermal energy into electrical power. It is defined as:[53] $ZT = \frac{S^2\sigma T}{\kappa}$, where S denotes the Seebeck coefficient, σ is the electrical conductivity, T is the absolute temperature, and $\kappa = \kappa_e + \kappa_l$ represents the total thermal conductivity, including electronic and lattice contributions. Efficient thermoelectric performance requires a suitable compromise between a high Seebeck coefficient, sufficient electrical conductivity, and low thermal conductivity. Fig. 8 present the

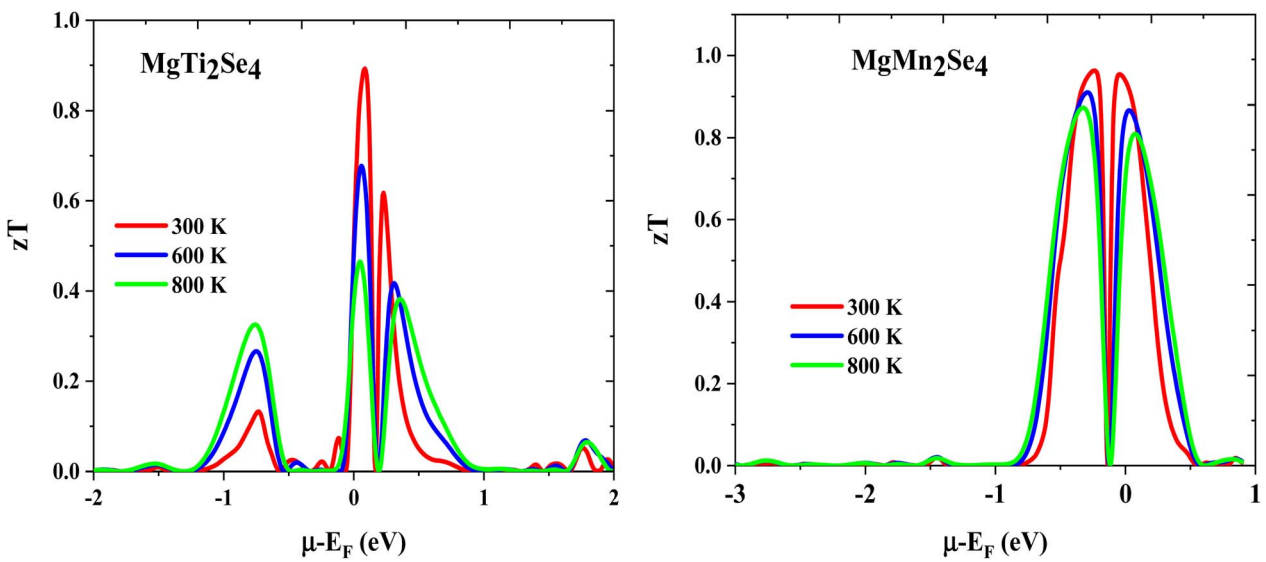

Fig. 8 Variation of the dimensionless thermoelectric figure of merit (ZT) as a function of chemical potential at different temperatures.

calculated variation of ZT as a function of chemical potential (μ–E_F) for $MgTi_2Se_4$ and $MgMn_2Se_4$ at temperatures of 300, 600, and 800 K. Since zT incorporates the combined effects of charge transport and heat conduction, it provides a comprehensive measure of thermoelectric performance. For both compounds, the zT profiles are strongly asymmetric with respect to the chemical potential. In the negative chemical potential region (μ–E_F < 0), corresponding to p-type doping, zT values remain very small over the entire investigated range and do not exhibit any pronounced maxima. In contrast, the positive chemical potential region shows well-defined zT peaks, indicating that thermoelectric performance is dominated by n-type charge carriers. For $MgMn_2Se_4$ at 300 K, the main ZT maximum is in the range μ–$E_F \approx$ 1.0–1.3 eV, with peak values approaching unity (0.99). As the temperature increases to 600 K and 800 K, the position of the maximum remains nearly unchanged, while the zT peak becomes slightly broader, suggesting an expanded chemical potential window for favorable n-type transport. A comparable trend is observed for $MgTi_2Se_4$. At room temperature, the zT curve exhibits a dominant n-type peak in the vicinity of μ–$E_F \approx -1.0$ to 1 eV, with maximum zT values slightly below unity (0.9). With increasing temperature, the peak height shows only a modest change, whereas the width of the zT peak increases gradually, indicating enhanced thermoelectric response over a wider doping range. Throughout the studied temperature range, zT values on the p-type side remain negligible in comparison to those on the n-type side. The concentration of the zT maxima near the conduction-band edge indicates that moderate n-type doping is required to achieve an optimal balance between the Seebeck coefficient and electrical conductivity. Away from this region, zT decreases rapidly due to the combined effects of reduced Seebeck coefficient and increased electronic thermal conductivity. The slight broadening of the ZT peaks with temperature can be attributed to thermal smearing of the electronic states and the temperature dependence of the transport coefficients. Overall, the consistently higher ZT values obtained under n-type conditions, particularly at elevated temperatures, indicate that $MgTi_2Se_4$ and $MgMn_2Se_4$ are more suitable for n-type thermoelectric applications than for p-type operation.

3.7 Phonon dynamics

The vibrational and dynamical stability of the spinel compounds $MgTi_2Se_4$ and $MgMn_2Se_4$ was systematically examined by calculating their phonon dispersion relations within the framework of density functional perturbation theory (DFPT), as implemented in the *Quantum ESPRESSO* package.[59] To accurately capture long-range interatomic interactions and lattice dynamics the interatomic force constants (IFCs) were computed using a 2 × 2 × 2 supercell combined with a 3 × 3 × 3 q-point mesh in the Brillouin zone. The exchange–correlation effects were treated within the generalized gradient approximation (GGA) which provides a reliable description of lattice vibrations and bonding characteristics in transition-metal chalcogenides. The primitive unit cell of MgX_2Se_4 (X = Ti, Mn) contains seven atoms giving rise to 21 phonon branches including three acoustic and eighteen optical modes, as depicted in Fig. 9. Group-theoretical analysis of the zone-center (Γ-point) vibrations based on the cubic spinel structure (space group $Fd\bar{3}m$, No. 227) yields the irreducible representation $\Gamma = 7E_u + 3A_{2u} + 5T_g + 3T_u + 2E_g + A_{1g}$. Several modes, namely E_u, T_g, T_u, and E_g, are degenerate due to the high cubic symmetry. In terms of optical activity, A_{1g}, E_g, and T_{2g} modes are Raman-active while T_{1u} modes are infrared-active. The remaining A_{2u}, E_u, and T_{2u} modes are optically silent. Although Raman and infrared measurements are not reported here the vibrational mode assignment is rigorously determined from group-

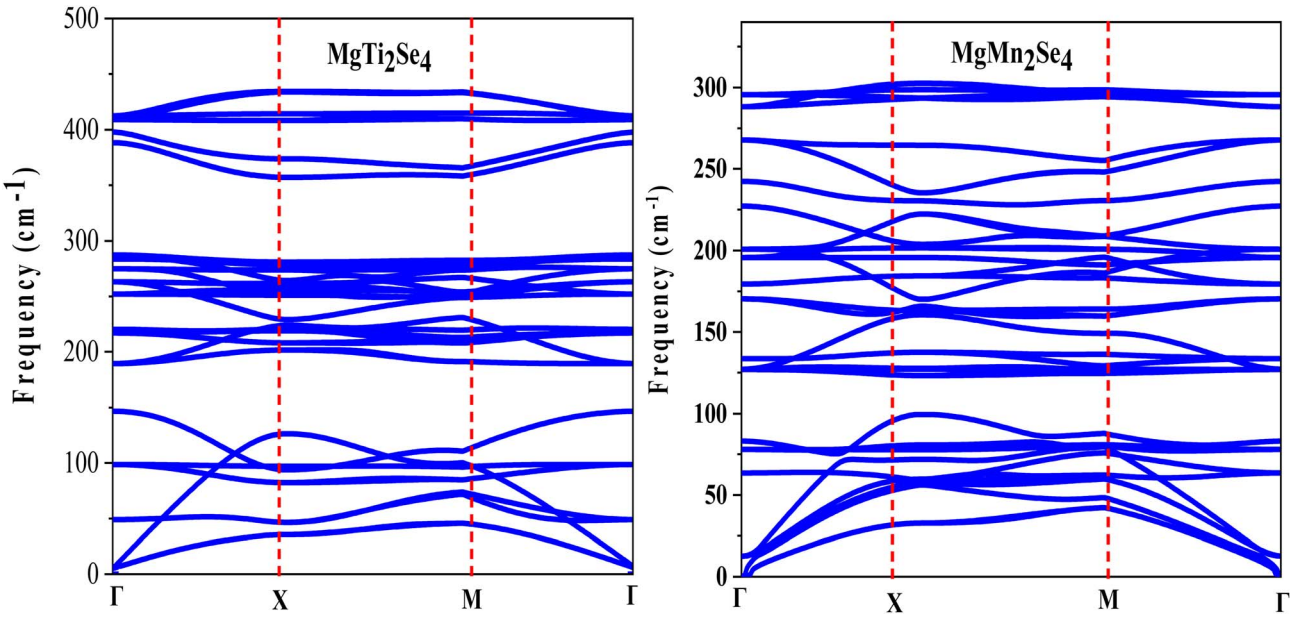

Fig. 9 Phonons dispersion plots of MgX_2Se_4(X = Ti/Mn).

theoretical symmetry considerations. The calculated phonon dispersion curves for both compounds show a complete absence of imaginary (negative) frequencies throughout the Brillouin zone confirming their dynamical stability at 300 K. Combined with their negative formation enthalpies this result establishes that $MgTi_2Se_4$ and $MgMn_2Se_4$ are stable both thermodynamically and against lattice instabilities. A detailed inspection of the phonon spectra provides microscopic insight into the lattice dynamics. In $MgTi_2Se_4$ the low-frequency region up to ~150 cm^{-1} is dominated by acoustic modes mainly arising from translational vibrations of Mg atoms reflecting their relatively weak bonding environment. The intermediate frequency ranges from ~180 to 290 cm^{-1} is primarily governed by vibrational modes of Ti atoms indicating strong coupling between Ti and the surrounding Se framework. The high-frequency optical modes spanning ~360–440 cm^{-1} are mainly due to Ti–Se stretching vibrations reflecting enhanced bond stiffness and increased covalent character within the Ti–Se network. In contrast, for $MgMn_2Se_4$ the acoustic branches extend up to ~90 cm^{-1} and are dominated by Mg-related translational motions. The intermediate frequency ranges from ~130 to 200 cm^{-1} is mainly associated with Mn-centered vibrations, while the high-frequency optical modes between ~240 and 320 cm^{-1} originate primarily from Mn–Se stretching vibrations. The comparatively lower maximum phonon frequencies in $MgMn_2Se_4$ reflect the larger atomic mass of Mn and relatively weaker Mn–Se bonding compared to the Ti–Se bonds in $MgTi_2Se_4$. These high-frequency optical phonons play a crucial role in determining electron–phonon coupling, charge-carrier scattering, and thermal transport properties. In both compounds, the separation between acoustic and optical branches and the relatively low dispersion of optical modes are expected to contribute to suppressed lattice thermal conductivity, which is highly desirable for thermoelectric applications.[60] Moreover, the coexistence of light Mg-dominated acoustic modes and stiffer transition-metal–Se optical modes promote enhanced phonon scattering, thereby reducing heat transport without significantly compromising electronic conductivity. Overall, the phonon dispersion analysis not only confirms the dynamical stability of $MgTi_2Se_4$ and $MgMn_2Se_4$ but also provides valuable insight into the interplay between atomic mass, bonding strength, and lattice vibrations. These characteristics are directly linked to their favorable thermal and electronic transport behavior, reinforcing their potential as promising candidates for spin-dependent thermoelectric and multifunctional device applications.

3.8 Electron density

In this work, we investigate charge sharing and bonding interactions among the constituent atoms by analysing the electron density distributions of magnesium-based transition-metal chalcogenides, namely $MgTi_2Se_4$ and $MgMn_2Se_4$, along the (001) crystallographic plane, as shown in Fig. 10. Covalent bonding interactions are indicated by the distinct overlapping

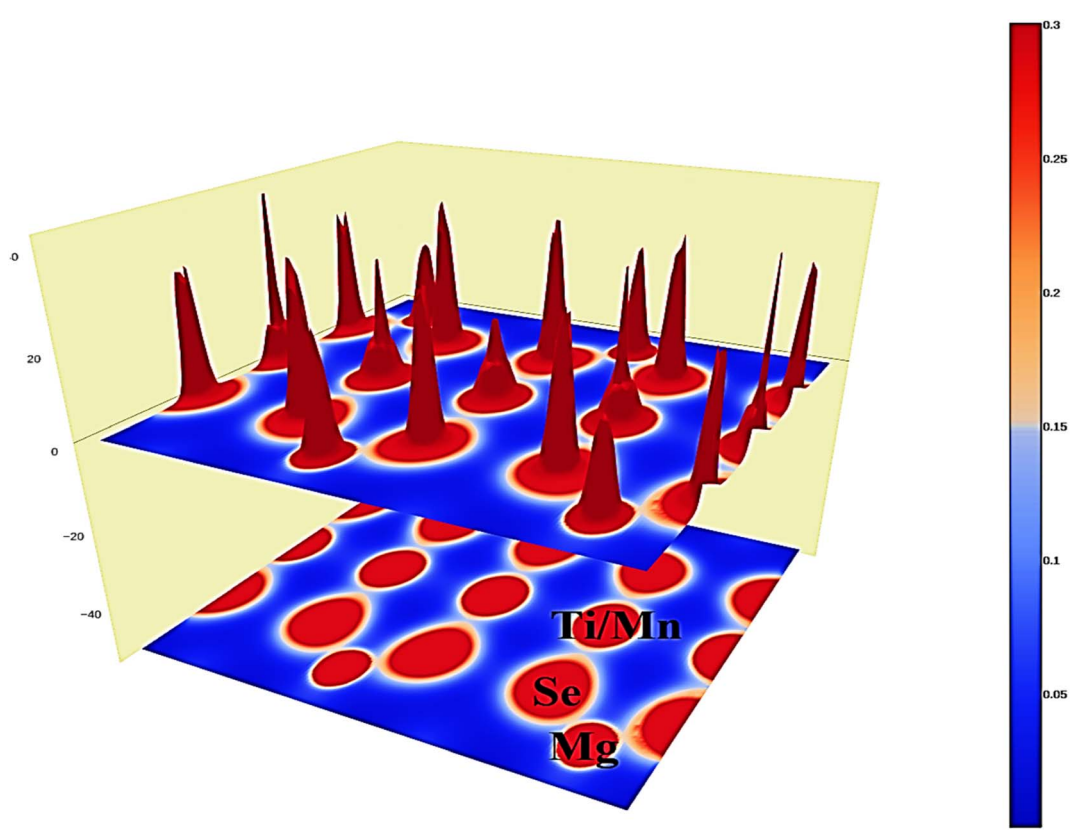

Fig. 10 Plot of electron density plots of (001) plane for $MgTi/Mn_2Se_4$.

charge regions between Ti/Mn and Se, as well as between Mg and Se, that are visible in the electron density maps. These maps clarify the bonding type and general structural stability of these spinel compounds by offering important insights into the dynamics of charge transfer between the cations (Mg and Ti/Mn) and the anion (Se). We computed the differences in electronegativity between the cations and anions to further evaluate the bonding properties. For Ti–Se and Mn–Se, the differences are 0.66 and 0.69, respectively, whereas for Mg–Se, the value is 1.24. These values validate the primarily covalent bonding character with slight ionic polarization because they fall below the critical threshold of 2.0. This suggests that the bonds in $MgTi_2Se_4$ and $MgMn_2Se_4$ are mixed ionic–covalent, with the covalent component greatly enhancing the materials' stability and electronic properties and the ionic contribution resulting from the metal–chalcogen separation.

4 Conclusion

This study presents a systematic first-principles investigation of the spinel chalcogenides $MgTi_2Se_4$ and $MgMn_2Se_4$ using density functional theory. Both compounds exhibit thermodynamic, dynamic, and mechanical stability. The ferromagnetic phase is energetically favored. The electronic structure reveals half-metallic behaviour with 100% spin polarization at the Fermi level, arising from strong hybridization between transition-metal-d and Se-p orbitals. This half-metallicity is accompanied by integer total magnetic moments of 4 μ_B per formula unit for $MgTi_2Se_4$ and 16 μ_B per formula unit for $MgMn_2Se_4$, confirming their half-metallic ferromagnetic nature. Elastic constant analysis demonstrates that both materials satisfy the Born stability criteria. They exhibit intrinsic ductility and pronounced elastic anisotropy. Enhanced lattice rigidity is further evidenced by high elastic moduli and Debye temperatures. Optical property analysis indicates strong electron–photon coupling. This behavior is characterized by large static dielectric constants, intense interband transitions, and efficient ultraviolet absorption with high optical conductivity. Spin-resolved thermoelectric transport calculations reveal favorable Seebeck coefficients, suppressed lattice thermal conductivity, and dominant majority-spin carrier transport. As a result, the dimensionless thermoelectric figure of merit reaches $ZT \approx 0.9$ for $MgTi_2Se_4$ and $ZT \approx 0.99$ for $MgMn_2Se_4$ near room temperature under n-type doping. The coexistence of half-metallicity, robust mechanical stability, strong optical response, and high thermoelectric efficiency establishes $MgTi_2Se_4$ and $MgMn_2Se_4$ as promising multifunctional materials. These features make them suitable for spintronic, spin-caloritronic, and energy-harvesting application

Conflicts of interest

The authors declare no competing interests.

Data availability

The data that support the findings of this study are available from the corresponding author upon reasonable request.

References

1 T. Naito, *Functional Materials: Advances and Applications in Energy Storage and Conversion*, Jenny Stanford Publishing, 1st edn, 2018.
2 A. Hirohata, K. Yamada, Y. Nakatani, I. L. Prejbeanu, B. Dieny, P. Pirro and B. Hillebrands, Review on spintronics: principles and device applications, *J. Magn. Magn. Mater.*, 2020, **509**, 166711.
3 W. Zeng, L. Shu, Q. Li, S. Chen, F. Wang and X. M. Tao, Fiber-based wearable electronics: a review of materials, fabrication, devices, and applications, *Adv. Mater.*, 2014, **26**, 5310–5336.
4 F. Ozel, *et al.*, A general review on the thiospinels and their energy applications, *Mater. Today Energy*, 2021, **21**, 100822.
5 R. M. Fleming, F. J. DiSalvo, R. J. Cava and J. V. Waszczak, Observation of charge-density waves in the cubic spinel structure CuV_2S_4, *Phys. Rev. B: Condens. Matter Mater. Phys.*, 1981, **24**, 2850–2853.
6 F. K. Lotgering and R. P. Van Stapele, Magnetic properties and electrical conduction of copper-containing sulfo- and selenospinels, *J. Appl. Phys.*, 1968, **39**, 417–423.
7 N. H. Van Maaren, G. M. Schaeffer and F. K. Lotgering, Superconductivity in sulpho- and selenospinels, *Phys. Lett. A*, 1967, **25**, 238–239.
8 F. Majid, M. T. Naisr, E. Algrafy, M. Sajjad, N. A. Noor, A. Mahmood and S. M. Ramay, Optical and magnetic properties of thiospinels for multifunctional applications, *J. Mater. Res. Technol.*, 2020, **9**, 6135–6142.
9 N. Imanishi, K. Inoue, Y. Takeda and O. Yamamoto, Thiospinels as cathode for lithium secondary battery, *J. Power Sources*, 1993, **44**, 619–625.
10 S. A. Abbas, I. Mahmood, M. Sajjad, N. A. Noor, Q. Mahmood, M. A. Naeem, A. Mahmood and S. M. Ramay, Spinel-type Na_2MoO_4 and Na_2WO_4 as promising optoelectronic materials: first-principles DFT calculations, *Chem. Phys.*, 2020, **538**, 110902.
11 G. J. Snyder, T. Caillat and J. P. Fleurial, Thermoelectric properties of chalcogenides with the spinel structure, *Mater. Res. Innov.*, 2001, **5**, 67–73.
12 K. Hashikuni, K. Suekuni, H. Usui, M. Ohta, K. Kuroki and T. Takabatake, High power factor in thiospinels $Cu_2TrTi_3S_8$ (Tr = Mn, Fe, Co, Ni) arising from TiS_6 octahedron network, *Appl. Phys. Lett.*, 2016, **109**, 182110.
13 M. Yousaf, S. A. Dalhatu, G. Murtaza, R. Khenata, M. Sajjad, A. Musa, H. A. R. Aliabad and M. A. Saeed, Optoelectronic properties of XIn_2S_4 (X = Cd, Mg) thiospinels through highly accurate all-electron FP-LAPW method, *J. Alloys Compd.*, 2015, **625**, 182–187.
14 O. Volnianska and P. Bogusławski, Magnetic and structural properties of IIA–V nitrides, *Phys. Rev. B: Condens. Matter Mater. Phys.*, 2007, **75**, 224418.

15 G. M. Mustafa, A. Ayaz, N. A. Noor, S. Mumtaz, A. Laref and A. Ibrahim, Theoretical investigation of semiconducting $CdTi_2X_4$ (X = S, Se) ferromagnetic spinels as multifunctional energy materials, *Results Eng.*, 2025, 107311.
16 H. A. Alburaih, N. A. Noor, M. Bououdina, H. Ullah, A. Laref and R. Sharma, First-principles study of Mg-based rare-earth spinels $MgSm_2Y_4$ (Y = S, Se) for spintronic and thermoelectric devices, *Mater. Chem. Phys.*, 2024, **313**, 128756.
17 G. M. Mustafa, B. Younas, S. Saba, N. A. Noor, Y. Saeed, S. Mumtaz and M. K. Al-Sadoon, Half-metallic ferromagnetic and transport behavior of rare-earth-based $CdGd_2(S/Se)_4$ spinels, *Mater. Today Commun.*, 2024, **40**, 109567.
18 Q. Mahmood, M. Hassan, G. Murtaza, M. Sajjad, A. Laref and B. Haq, Theoretical investigation of electronic, magnetic, and thermoelectric behavior of LiZ_2O_4 (Z = Mn, Fe, Co, Ni), *J. Supercond. Novel Magn.*, 2019, **32**, 1231–1239.
19 T. H. Flemban, V. Singaravelu, A. A. S. Devi and I. S. Roqan, Homogeneous vertical ZnO nanorod arrays with high conductivity on an *in situ* Gd nanolayer, *RSC Adv.*, 2015, **5**, 94670–94678.
20 R. A. de Groot, F. M. Mueller, P. G. van Engen and K. H. J. Buschow, New class of materials: half-metallic ferromagnets, *Phys. Rev. Lett.*, 1983, **50**, 2024.
21 J. M. D. Coey and M. Venkatesan, Half-metallic ferromagnetism: example of CrO_2, *J. Appl. Phys.*, 2002, **91**, 8345.
22 M. Horne, P. Strange, W. M. Temmerman, Z. Szotek, A. Svane and H. Winter, Electronic structure of europium chalcogenides and pnictides, *J. Phys.: Condens. Matter*, 2004, **16**, 5061.
23 Y. Lang, L. Pan, C. Chen and Y. Wang, Thermoelectric properties of thiospinel-type $CuCo_2S_4$, *J. Electron. Mater.*, 2019, **48**, 4179–4187.
24 W. Tahir, G. M. Mustafa, N. A. Noor, S. M. Alay-e-Abbas, Q. Mahmood and A. Laref, Analysis of optoelectronic and transport properties of magnesium-based $MgSc_2X_4$ (X = S, Se) spinels, *Ceram. Int.*, 2020, **46**, 26637–26645.
25 G. M. Mustafa, S. Saba, N. A. Noor, A. Laref, M. Abd El-Rahman, Z. Farooq, R. B. Behram and Z. Ullah, First-principles calculations to investigate $HgY_2(S/Se)_4$ spinel chalcogenides, *J. Mater. Res. Technol.*, 2023, **22**, 97–106.
26 N. A. Noor, M. Rashid, G. M. Mustafa, A. Mahmood, W. Al-Masry and S. M. Ramay, Zinc-based chalcogenides $ZnMn_2X_4$ (X = S, Se, Te) as promising spintronic materials, *J. Alloys Compd.*, 2021, **856**, 157198.
27 G. M. Mustafa, N. A. Noor, M. W. Iqbal, M. Sajjad, M. A. Naeem, Q. Mahmood, H. M. Shaikh, A. Mahmood and W. Al-Masry, Optoelectronic and transport properties of $MgLu_2Z_4$ (Z = S, Se) spinels, *Mater. Sci. Semicond. Process.*, 2021, **121**, 105452.
28 G. M. Mustafa, T. Zelai, S. Bouzgarrou, M. H. Alhossainy, Q. Mahmood, A. Mera, H. H. Hegazy, S. Alharthi and M. A. Amin, First-principles study of magnesium-based $MgLa_2(S/Se)_4$ chalcogenides, *Appl. Phys. A*, 2022, **128**, 38.
29 A. Ramzan, M. Y. Sofi, M. Ishfaq-ul-Islam, M. S. Khan and M. A. Khan, Half-metallic ferromagnetism and thermoelectric-efficient behavior in $MgNi_2X_4$ (X = S, Se) spinels, *RSC Adv.*, 2025, **15**, 24002–24018.
30 S. A. Rouf, H. Albalawi, T. Zelai and O. Hakami, Half-metallic ferromagnetism and thermoelectric effect in SrX_2S_4 (X = Mn, Fe, Co), *J. Phys. Chem. Solids*, 2023, **182**, 111601.
31 Q. Mahmood, G. Nazir, J. Alzahrani and N. A. Kattan, Room temperature ferromagnetism and thermoelectric behavior of calcium-based spinel chalcogenides CaZ_2S_4 (Z = Ti, V, Cr, Fe), *J. Phys. Chem. Solids*, 2022, **167**, 110742.
32 P. Blaha, K. Schwarz, G. K. H. Madsen, D. Kvasnicka, J. Luitz, R. Laskowski, F. Tran and L. D. Marks, *WIEN2k: an Augmented Plane Wave Plus Local Orbitals Program for Calculating Crystal Properties*, Technische Universität Wien, 2019.
33 J. P. Perdew, K. Burke and M. Ernzerhof, Generalized gradient approximation made simple, *Phys. Rev. Lett.*, 1996, **77**, 3865.
34 D. Koller, F. Tran and P. Blaha, Improving the modified Becke–Johnson exchange potential, *Phys. Rev. B: Condens. Matter Mater. Phys.*, 2012, **85**, 155109.
35 G. K. H. Madsen and D. J. Singh, BoltzTraP: a code for calculating band-structure-dependent quantities, *Comput. Phys. Commun.*, 2006, **175**, 67–71.
36 M. Y. Sofi, M. S. Khan and M. A. Khan, Semiconducting ferromagnetism and thermoelectric performance of Rb_2GeMI_6 (M = V, Ni, Mn), *Mater. Adv*, 2025, **6**, 2071–2089.
37 A. Ramzan, M. Y. Sofi, M. S. Khan, J. Ali and M. A. Khan, First-principles investigation of $MgAl_2X_4$ (X = S, Se) spinels, *Eur. Phys. J. B*, 2025, **98**, 102.
38 F. D. Murnaghan, The compressibility of media under extreme pressures, *Proc. Natl. Acad. Sci. U. S. A.*, 1944, **30**, 244–247.
39 M. Khalid, M. W. Iqbal, M. Asghar, N. A. Noor, G. M. Mustafa and S. M. Ramay, Exchange mechanism and transport characteristics of Mg-based spinel chalcogenides, *Eur. Phys. J. Plus*, 2022, **137**, 1.
40 Z. Szotek, W. M. Temmerman, A. Svane, L. Petit, P. Strange, G. M. Stocks, D. Kodderitzsch, W. Hergert and H. Winter, Electronic structure of half-metallic ferromagnets and spinel ferromagnetic insulators, *J. Phys.: Condens. Matter*, 2004, **16**, S5587–S5600.
41 A. Mahmood, S. M. Ramay, W. Al-Masry, C. W. Dunnill and N. Y. Al-Garadi, First-principles computations of ferromagnetic $HgCr_2Z_4$ (Z = S, Se) spinels, *J. Mater. Res. Technol.*, 2020, **9**, 16159–16166.
42 G. M. Mustafa, A. Ayaz, N. A. Noor, S. Mumtaz, A. Laref and A. Ibrahim, Semiconducting $CdTi_2X_4$ (X = S, Se) ferromagnetic spinels, *Results Eng.*, 2025, 107311.
43 R. Trivedi and B. Chakroborty, Design of room-temperature d^0 ferromagnetism for spintronics applications, in *Fundamentals of Low Dimensional Magnets*, CRC Press, 2022, pp. 161–182.
44 H. Yilin, W. Yang, L. Tingzhou, Y. Tie and W. Xiaotian, Electronic, magnetic, half-metallic, and mechanical

properties of equiatomic quaternary Heusler compound YRhTiGe, *Materials*, 2018, **11**, 797.

45 H. Peng, H. J. Xiang, S.-H. Wei, S.-S. Li, J.-B. Xia and J. Li, Origin and enhancement of hole-induced ferromagnetism in first-row d^0 semiconductors, *Phys. Rev. Lett.*, 2009, **102**, 017201.

46 M. Born, On the stability of crystal lattices, *Math. Proc. Cambridge Philos. Soc.*, 1940, **36**, 160.

47 W. Voigt, *Textbook of Crystal Physics, G. B*, Teubner, 1928.

48 A. Reuss, Calculation of the flow limit of mixed crystals, *Z. Angew. Math. Mech.*, 1929, **9**, 49–58.

49 R. Hill, The elastic behaviour of a crystalline aggregate, *Proc. Phys. Soc. A*, 1952, **65**, 349.

50 S. I. Ranganathan and M. Ostoja-Starzewski, Universal elastic anisotropy index, *Phys. Rev. Lett.*, 2008, **101**, 055504.

51 S. A. Raza, G. M. Mustafa, M. A. Ameer, N. A. Noor, Z. Farooq, S. Mumtaz and I. M. Moussa, Investigation of $MnSc_2X_4$ (X = S, Se) spinels, *RSC Adv.*, 2025, **15**, 9662–9675.

52 T. Alshahrani, G. M. Mustafa, T. H. Flemban, H. Althib, S. Al-Qaisi, N. A. Kattan and Q. Mahmood, Optoelectronic and transport properties of ZnY_2X_4 (X = S, Se) spinels, *ECS J. Solid State Sci. Technol.*, 2020, **9**, 105001.

53 M. Y. Sofi, M. S. Khan and M. A. Khan, Eco-friendly lead-free halide double perovskites A_2CuMCl_6 (A = K, Rb; M = Sb, Bi), *J. Mater. Chem. C*, 2024, **12**, 16045–16058.

54 M. Y. Sofi, M. S. Khan and M. A. Khan, Harnessing half-metallicity and thermoelectric insights in Cs_2AgMBr_6 (M = V, Mn, Ni), *Mater. Sci. Semicond. Process.*, 2025, **186**, 109023.

55 Q. Mahmood, G. M. Mustafa, B. Younas, S. Bouzgarrou, A. I. Aljameel, M. H. Mashniwi, M. Y. Almashnowi and N. Sfina, Structural, magnetic, and thermoelectric properties of $CdCe_2X_4$ (X = S, Se, Te) spinels, *J. Phys. Chem. Solids*, 2025, **197**, 112433.

56 M. Furqan, G. M. Mustafa, H. D. Alkhaldi, F. Alhajri, G. I. Ameereh, M. Al-Anazy, A. El-Rayyes and Q. Mahmood, Electronic, magnetic, and thermoelectric aspects of $SrCe_2Z_4$ (Z = Te, Se, S), *RSC Adv.*, 2025, **15**, 37288–37298.

57 G. A. Slack, Non-metallic crystals with high thermal conductivity, *J. Phys. Chem. Solids*, 1973, **34**, 321–335.

58 M. Y. Sofi, M. S. Khan, J. Ali and M. A. Khan, Role of 3d electrons in ferromagnetism and spin-dependent transport in K_2GeNiX_6 (X = Br, I), *J. Phys. Chem. Solids*, 2024, **192**, 112022.

59 P. Giannozzi, *et al.*, QUANTUM ESPRESSO: a modular and open-source software project for quantum simulations of materials, *J. Phys.: Condens. Matter*, 2009, **21**, 395502.

60 M. Y. Sofi, M. S. Khan and M. A. Khan, Control of spin on ferromagnetism and thermoelectric properties of K_2GeMnX_6 (X = Cl, Br, I), *Mater. Adv.*, 2024, **5**, 4913–4931.